Nucleation studies in the Martian atmosphere

A. Määttänen, H. Vehkamäki, and A. Lauri
Division of Atmospheric Sciences, Department of Physical Sciences, University of Helsinki, Helsinki, Finland

S. Merikallio
Space Research, Finnish Meteorological Institute, Helsinki, Finland

J. Kauhanen, H. Savijärvi, and M. Kulmala
Division of Atmospheric Sciences, Department of Physical Sciences, University of Helsinki, Helsinki, Finland

Received 15 June 2004; revised 18 November 2004; accepted 1 December 2004; published 5 February 2005.

[1] We developed models for unary nucleation of water and carbon dioxide in the Martian atmosphere. Both homogeneous and heterogeneous nucleation on dust particles were studied. Our models are based on classical theory. We compare results of different adsorption approaches. Heterogeneous nucleation on the abundant dust particles seems to be the primary mechanism of both H_2O and CO_2 cloud formation in the Martian atmosphere. Heterogeneous nucleation is obtained at a saturation ratio of about 1.18 for H_2O and 1.32 for CO_2. Homogeneous nucleation is not likely to occur since it would require high supersaturations. We use our models to study nucleation as a function of height at different locations on Mars where ice fog or clouds have been observed. H_2O ice nucleation results are in good agreement with surface fog observations and previous model studies. CO_2 ice nucleation simulations in the polar hood cloud areas suggest that negative temperature perturbations caused by, e.g., adiabatic cooling in orographic waves or in convective plumes are required for the formation of CO_2 clouds.

Citation: Määttänen, A., H. Vehkamäki, A. Lauri, S. Merikallio, J. Kauhanen, H. Savijärvi, and M. Kulmala (2005), Nucleation studies in the Martian atmosphere, *J. Geophys. Res.*, *110*, E02002, doi:10.1029/2004JE002308.

1. Introduction

[2] The Martian atmosphere is thin, cold, and dry but presents similar meteorological phenomena as the atmosphere on Earth. The planet also exhibits similar seasons (though longer) and diurnal variations (though stronger) as those found on Earth. Dust is abundant on Mars and one of the most visible phenomena are the global dust storms that quasi-regularly cover the entire planet with a red veil. Clouds formed by both carbon dioxide and water ice crystals have been observed in the Martian atmosphere by satellite as well as by telescope. Clouds and dust are connected via the capability of dust particles to function as cloud condensation nuclei.

[3] The aim of this study was to find a consistent way of analyzing cloud particle formation under Martian conditions. We worked on the first step of cloud formation, nucleation, and used classical nucleation theory, which has been examined theoretically by, for instance, *Lazaridis et al.* [1991] and *Kulmala et al.* [2001]. Several theoretical studies on the formation of clouds on Mars have previously been conducted [*Michelangeli et al.*, 1993; *Colaprete et al.*, 1999; *Wood*, 1999; *Inada*, 2002]. Our models include the two major nucleating substances, H_2O and CO_2, and we have also taken into account the nonisothermal effects that become important when the gas involved is a major constituent of the atmosphere. We used temperature and moisture profiles acquired from the Mars Climate Database (MCD) [*Lewis et al.*, 1999] and the one-dimensional (1-D) model of *Savijärvi* [1999] and *Savijärvi et al.* [2004] in an attempt to model nucleation in locations where surface fog or cloud formation have been observed, as in the Mars Pathfinder landing area [*Schofield et al.*, 1997] and the Memnonia region [*Briggs et al.*, 1977]. The Mars Pathfinder entry profile was used as by *Colaprete et al.* [1999] to investigate cloud formation. Polar hood cloud areas were also investigated using atmospheric profiles obtained from the MCD. Results were compared with observations and other model studies.

0148-0227/05/2004JE002308$09.00

2. Theory and Model Descriptions

2.1. Homogeneous Nucleation Theory

[4] Stable clusters (large enough for their growth to be thermodynamically favored) of molecules form directly from the vapor phase with homogeneous nucleation. The free energy of formation of a spherical cluster with radius r is given by the Gibbs-Thompson equation

$$\Delta F_{\mathrm{hom}} = -\frac{4\pi r^3}{3v_i} kT \ln S + 4\pi r^2 \sigma, \qquad (1)$$

where $v_i = m_m/\rho_i$ is the molecular volume in the condensed phase, m_m the mass of a molecule, ρ_i the density of the

condensed phase, T the temperature, k the Boltzmann constant, σ the surface tension, and S the saturation ratio. A detailed description of the theory is given by *Volmer* [1939], *Fletcher* [1958], *Keesee* [1989], and *Pruppacher and Klett* [1997]. The critical free energy of formation

$$\Delta F^*_{\text{hom}} = \frac{16\pi v_i^2 \sigma^3}{3(kT \ln S)^2} \tag{2}$$

and the radius of the critical cluster

$$r^* = \frac{2v_i\sigma}{kT \ln S} \tag{3}$$

are obtained from the zero-point of the derivative of the Gibbs-Thompson equation (equation (1)).

[5] The classical homogeneous nucleation rate (as new particles per unit volume and unit time) is given by

$$\begin{aligned} J_{\text{hom}} &= f_{\delta T} Z_{\text{hom}} \beta^*_{\text{hom}} c_{1,v} \exp\left(\frac{-\Delta F^*_{\text{hom}}}{kT}\right) \\ &= f_{\delta T} \left(\frac{\Delta F^*_{\text{hom}}}{3\pi kT n^{*2}}\right)^{1/2} \left(4\pi r^{*2} \sqrt{\frac{kT}{2\pi m_m}}\right) c_{1,v}^2 \exp\left(\frac{-\Delta F^*_{\text{hom}}}{kT}\right), \end{aligned} \tag{4}$$

which describes the collision rate of vapor molecules with nuclei of critical size. The term in the first brackets is the Zeldovich factor $Z_{\text{hom}} = \left(\frac{\Delta F^*_{\text{hom}}}{3\pi kTn^{*2}}\right)^{1/2}$, where n^* is the number of molecules in the critical cluster. The Zeldovich factor accounts for the difference between critical cluster concentration in the nucleating vapor and equilibrium vapor and break-up of critical clusters. $f_{\delta T}$ is the nonisothermal coefficient which will be described in section 2.4. $c_{1,v}$ is the vapor concentration (number of monomers in the vapor phase). $\beta^*_{\text{hom}} = c_{1,v} 4\pi r^{*2} \sqrt{\frac{kT}{2\pi m_m}}$ is the rate at which monomers collide with a critical cluster.

2.2. Heterogeneous Nucleation Theory Used in the Models

[6] Heterogeneous nucleation describes the nucleation of critical clusters on a substrate, which on Mars is the ubiquitous and abundant airborne mineral dust. When a species nucleates on a substrate, the surface energy per molecule is reduced, thus enabling an equilibrium cluster with a certain amount of molecules to have a larger radius of curvature. The nucleating vapor forms a cap that makes contact with the underlying surface at an angle θ, which can be determined from mechanical equilibrium in terms of interfacial energies

$$m = \cos\theta = \frac{\sigma_{\text{CN/v}} - \sigma_{\text{CN/i}}}{\sigma_{\text{i/v}}}, \tag{5}$$

where $\sigma_{\text{i/j}}$ is the interfacial tension between phases i and j, CN the condensation nucleus, v the vapor, and i the ice. For a given contact parameter m, the free energy of formation of a critical cluster on a spherical substrate is reduced from the homogeneous case (equation (2)) by a factor f [*Fletcher*, 1958]:

$$\begin{aligned} 2f = 1 &+ \left(\frac{1 - Xm}{g}\right)^3 + X^3 \left[2 - 3\left(\frac{X - m}{g}\right) + \left(\frac{X - m}{g}\right)^3\right] \\ &+ 3X^2 m \left(\frac{X - m}{g} - 1\right), \end{aligned} \tag{6}$$

where $g = (1 + X^2 - 2Xm)^{1/2}$ and $X = r_{\text{CN}}/r^*$, the latter being a size parameter giving the ratio of the radius of the CN (r_{CN}) to the radius of the critical cluster. For heterogeneous nucleation, there are several ways that the nucleation rate can be calculated. In the next sections, two cases will be reviewed.

2.2.1. Heterogeneous Nucleation by Surface Diffusion

[7] The surface diffusion approach for heterogeneous nucleation describes nucleation as a process where gas molecules (pressure $p_v = c_{1,v}kT$) collide with the CN and adhere to it. Diffusion on the surface then causes the monomers to form clusters of different sizes which may grow to the critical size. The surface concentration of the monomers, $c_{1,s}$, is described at steady-state calculated from the incoming and outgoing molecule fluxes [*Pruppacher and Klett*, 1997]

$$c_{1,s} = \frac{p_v}{(2\pi m_m kT)^{1/2} \nu} \exp[\Delta F_{\text{des}}/kT], \tag{7}$$

where ν is the vibrational frequency of the molecule on the surface and ΔF_{des} the energy for surface desorption. The heterogeneous nucleation rate (per CN surface area per second, units $\text{m}^{-2}\ \text{s}^{-1}$) can be expressed in the following form [*Keesee*, 1989]:

$$\begin{aligned} J_{\text{het}} &= f_{\delta T} Z_{\text{het}} \beta_{\text{het}} c_{1,s} \exp\left(\frac{-\Delta F^*_{\text{het}}}{kT}\right) \\ &= f_{\delta T} \frac{1}{\sqrt{f}} Z_{\text{hom}} 2\pi d\nu r^* \sin\theta c_{1,s}^2 \exp\left(\frac{-\Delta F_{\text{sd}} - f\Delta F^*_{\text{hom}}}{kT}\right) \\ &= f_{\delta T} \frac{Z_{\text{hom}} kTdr^* \sin\theta}{\sqrt{f}\nu m_m} c_{1,v}^2 \exp\left(\frac{2\Delta F_{\text{des}} - \Delta F_{\text{sd}} - f\Delta F^*_{\text{hom}}}{kT}\right), \end{aligned} \tag{8}$$

where ΔF_{sd} is the energy for surface diffusion and d the mean jump distance of a molecule. The term β_{het} is the product of the number of adsorbed water molecules in position to join the germ ($2\pi r^* \sin\theta d c_{1,s}$) and the frequency $\left(\nu \exp\left(\frac{-\Delta F_{\text{sd}}}{kT}\right)\right)$ with which the adsorbed molecule will jump to join the germ.

[8] Z_{hom}, the Zeldovich factor, is exactly the same as in the case of homogeneous nucleation. This formulation assumes that the number of molecules in the heterogeneous critical cluster (n^*_{het}) is obtained from that in the homogeneous cluster (n^*_{hom}) by multiplying with the factor f (equation (6)) to relate the free energies of the clusters, resulting in the $1/\sqrt{f}$ in the formula of J_{het} (equation (8)). This assumption is only true for nucleation occurring on a planar substrate. In the following, we derive a coefficient that should be used for calculating n^*_{het} from n^*_{hom} when nucleation takes place on a curved surface. *Fletcher* [1958] derived the volume of the embryo formed on a curved

surface in the heterogeneous case (Fletcher's equation (4)) which, using relations (5)–(9) of *Fletcher* [1958], can be written in the form

$$V^*_{\text{het}} = \frac{1}{3}\pi r^3 \left(2 + 3\left(\frac{1-Xm}{g}\right) - \left(\frac{1-Xm}{g}\right)^3 - X^3 \cdot \left(2 - 3\left(\frac{X-m}{g}\right) + \left(\frac{X-m}{g}\right)^3\right)\right), \quad (9)$$

where g, X, and m are as in equation (6). Thus we can derive a coefficient $f_{n*} = (n^*_{\text{het}}/n^*_{\text{hom}}) = (V^*_{\text{het}}/V^*_{\text{hom}})$ to be used for calculating n^* for heterogeneous nucleation on a curved surface. With $V^*_{\text{hom}} = (4/3)\pi r^{*3}$, we get

$$f_{n*} = \frac{1}{4}\left(2 + 3\left(\frac{1-Xm}{g}\right) - \left(\frac{1-Xm}{g}\right)^3 - X^3\left(2 - 3\left(\frac{X-m}{g}\right) + \left(\frac{X-m}{g}\right)^3\right)\right). \quad (10)$$

Now the Zeldovich factor Z_{het} for heterogeneous nucleation can be described with the help of Z_{hom} for the homogeneous case as

$$Z_{\text{het}} = \left(\frac{f\Delta F^*_{\text{hom}}}{3\pi kT\left(f_{n*}n^*_{\text{hom}}\right)^2}\right)^{1/2} = \frac{\sqrt{f}}{f_{n*}} \cdot \left(\frac{\Delta F^*_{\text{hom}}}{3\pi kTn^{*2}_{\text{hom}}}\right)^{1/2} = \frac{\sqrt{f}}{f_{n*}} \cdot Z_{\text{hom}}. \quad (11)$$

With this definition, we get the heterogeneous nucleation rate

$$J_{\text{het}} = f_{\delta T}\frac{Z_{\text{het}}kTdr^*\sin\theta}{\nu m_m}c^2_{1,v}\exp\left(\frac{2\Delta F_{\text{des}} - \Delta F_{\text{sd}} - f\Delta F^*_{\text{hom}}}{kT}\right), \quad (12)$$

where Z_{het} is the new formulation (equation (11)), including both f and f_{n*}, and f also appears in the exponential term as in equation (8).

[9] In the cases we studied with a monodisperse 1 μm CN distribution, the difference between formulae (8) and (12) (i.e., the difference between $1/\sqrt{f}$ and $\sqrt{f}/f_{n*}$) is not numerically significant. In the following simulations, we use the curved surface formulation, which is important to include in heterogeneous nucleation models, especially considering a small CN with a strong surface curvature.

2.2.2. Heterogeneous Nucleation by Direct Vapor Deposition

[10] The direct vapor deposition approach, compared with the previously described surface diffusion approach, takes into account only the monomer collisions hitting and adhering directly to the surface of the embryo on the CN.

[11] The approach used by, for example, *Inada* [2002] largely follows the formulation described here, the equations for the critical cluster free energy ΔF^*, the radius r^*, and the reduction factor f being the same as in equations (2), (3), and (6). Note that also when assuming direct vapor deposition we need to know the equilibrium concentration of critical clusters per substrate surface area, which has the form $c_{1,s}\exp\left(\frac{-f\Delta F^*_{\text{hom}}}{kT}\right)$, and thus the monomer concentration on the surface, $c_{1,s}$, is needed. In the study of *Inada* [2002], it is assumed that the entire surface of the CN is covered with a monolayer, the thickness of which is the diameter of one monomer,

$$c_{1,s} = \frac{2r_i}{v_i}, \quad (13)$$

where r_i is the radius and v_i the volume of a monomer, and the nucleation rate per CN surface area per second is

$$J_{\text{het}} = Z_{\text{het}}\beta_{\text{het}}c_{1,s}\exp\left(\frac{-\Delta F^*_{\text{het}}}{kT}\right) = \frac{\pi r^{*2}Z_{\text{het}}p_v}{\sqrt{2\pi m_m kT}}c_{1,s}\exp\left(\frac{-f\Delta F^*_{\text{hom}}}{kT}\right), \quad (14)$$

where $\beta_{\text{het}} = \left(\pi r^{*2}p_v\right)/\left(\sqrt{2\pi m_m kT}\right)$ is the rate of vapor molecule collision with the cup-shaped embryo, with the cap surface area approximated by πr^{*2}.

2.3. Thermodynamic Data

[12] For modeling one-component nucleation, the following thermodynamic data are required: saturation vapor pressure of the nucleating substance p_s, density of the nucleated phase ρ_i, surface tension or surface energy σ, molecular weight m_m, and molecular heat capacity c_p, and for heterogeneous nucleation also the contact angle θ (or the contact parameter $m = \cos\theta$) between the substrate and the condensation nucleus (CN), energies for surface diffusion ΔF_{sd} and desorption ΔF_{des}, mean jump distance d, and vibrational frequency ν of the molecule on the surface. The values used for these data and the related references are presented in Table 1.

[13] For Martian substances, satisfactory data exist for water since ice nucleation at high altitudes in Earth's atmosphere can be considered an analog to the water ice nucleation on Mars. However, because we lack knowledge about the exact composition of Martian dust particles, the best terrestrial analog for use in measurements of heterogeneous parameters is unknown.

[14] For CO_2, to our knowledge, only one set of measurements for nucleation in Martian conditions has been done to date [*Glandorf et al.*, 2002]. In their measurements, *Glandorf et al.* [2002] observed CO_2 nucleation on several sites on a 1 cm^2 water film during some seconds measuring the saturation ratio at the same time. They defined this critical nucleation rate as 1 $cm^{-2}s^{-1}$ and deducted the contact parameter from the results using classical nucleation theory. However, we have not presumed the dust particles to be already covered with water, or the water ice particles to act as condensation nuclei. Thus we had to evaluate the contact parameter between CO_2 and mineral dust. Comparing the results of *Glandorf et al.* [2002] with the derived contact parameters of water on mineral dust, we decided to use their value of $m = 0.952$ also for nucleation of CO_2 on dust. We reproduced the results of the experiment of *Glandorf et al.* [2002] with our model quite well; this will be briefly discussed in section 3.2.

[15] With H_2O, we used the value $m = 0.97$ evaluated by *Wood* [1999], which is close to the value of $m = 0.975$

Table 1. Parameters for Basic Cases of Homogeneous and Heterogeneous Nucleation

Parameter	Symbol	CO_2	H_2O
Contact parameter	m	0.952 [*Glandorf et al.*, 2002]	0.97 [*Wood*, 1999]
Energy of adsorption, J molecule^{-1}	ΔF_{des}	$3.25 \cdot 10^{-20}$ [*Zent and Quinn*, 1995]	$2.9 \cdot 10^{-20}$ [*Seki and Hasegawa*, 1983]
Energy of surface diffusion, J molecule^{-1}	ΔF_{sd}	$3.25 \cdot 10^{-21}$ [*Seki and Hasegawa*, 1983]	$2.9 \cdot 10^{-21}$ [*Seki and Hasegawa*, 1983]
Saturation vapor pressure, Pa	p_{sat}	[*Kasting*, 1991]	[*Buck*, 1981]
Surface energy, J m^{-2}	σ	0.080 [*Wood*, 1999]	0.106 [*Pruppacher and Klett*, 1997]
Ice density, kg m^{-3}	ρ_{ice}	1600.0 [*Wood*, 1999]	[*Pruppacher and Klett*, 1997]
Molecular heat capacity, J K^{-1}	c_v	6.166e−23 calculated	4.66e−23 calculated
Vibrational frequency of the molecule, s^{-1}	ν	$2.9 \cdot 10^{12}$ [*Sanford and Allamandola*, 1990]	$1.0 \cdot 10^{13}$ [*Pruppacher and Klett*, 1997]
Jumping distance of the molecule, m	d	$4.0 \cdot 10^{-10}$ [*Wood*, 1999]	$3.2 \cdot 10^{-10}$ [*Pruppacher and Klett*, 1997]
Dust optical depth	τ	0.1 [*Wood*, 1999]	
CN number density at the surface, m^{-3}	N_{CN}	$1.3 \cdot 10^{6}$ [*Wood*, 1999]	
Atmospheric pressure, Pa	p_{atm}	600.0	
Temperature range, K	T_{range}	$100 \leq T_{\mathrm{range}} \leq 300$	

applied by *Inada* [2002] and based on *Michelangeli et al.* [1993]. In the comparison with *Inada* [2002], we used their value. *Colaprete et al.* [1999] had used a value of $m = 0.95$, an average of the results of *Michelangeli et al.* [1993]. For the desorption and surface diffusion energies ΔF_{des} and ΔF_{sd}, we used values taken from *Wood* [1999, and references therein] for CO_2 and from *Seki and Hasegawa* [1983] for H_2O.

2.4. Nonisothermal Effects

[16] Our models include nonisothermal effects which become important when the nucleating species forms the majority of the atmosphere, as is the case for CO_2 on Mars (constituting 95.3% of the atmosphere). The nonisothermal coefficient is also calculated for water in our simulations, although the effect is not expected to be significant.

[17] The dimensionless nonisothermal factor $f_{\delta T}$ describes the reduction in the nucleation rate compared with the classical isothermal case [*Feder et al.*, 1966] when the amount of the inert carrier gas is very small and the nucleating species is abundant. With only a small amount of carrier gas, the forming clusters warm up significantly since the collisions of the nucleating gas are far more frequent than those of the inert gas molecules. Thus the heat of condensation is not effectively transported away from the cluster, and the cluster heats up. As a final consequence, the nucleation rate is slowed down by a factor $f_{\delta T}$ ($0 < f_{\delta T} < 1$). It is defined as

$$f_{\delta T} = \frac{b^2}{b^2 + q^2}, \tag{15}$$

where b describes the energy lost in collisions with gas molecules and q the energy gained with the molecules acquired to the cluster [*Feder et al.*, 1966]. The nonisothermal coefficient is a function of temperature and the ratio of the nucleating gas and the inert carrier gas. We do not use a constant, average value for the coefficient, unlike *Wood* [1999], who obtained a value of 0.006 for CO_2, but calculate it in the model during the simulations. The values obtained for $f_{\delta T}$ in our simulations vary between 0.966 and 1.0 for H_2O in the temperature range 107–200 K and between $1.3 \cdot 10^{-2}$ and $3.3 \cdot 10^{-2}$ for CO_2 in the temperature range 100–147 K. The difference of factor 10 to the result of *Wood* [1999] is difficult to trace due to lack of sufficient background information on his approach to the problem. We derived our coefficient independently using the theory of *Feder et al.* [1966] and the atmospheric composition included in our model (95.3% CO_2).

2.5. Presentation of Nucleation Rate

[18] For homogeneous nucleation, the traditional way of presenting the nucleation rate is in units cm^{-3} s^{-1} describing how many new particles are formed per unit time and unit volume. For heterogeneous nucleation, the convention is not well established and many different forms are used. Using the same units as for homogeneous nucleation is not very practical since the amount of condensation nuclei in the unit volume is critical and should also be known. Options for presenting J are, for example, to give the number of forming critical clusters per 1) unit area of condensation nuclei in unit time (m^{-2} s^{-1}) or 2) per particle (condensation nucleus) in unit time (s^{-1}). Also the nucleation probability

$$P = 1 - \exp(-J_{\mathrm{het}} t), \tag{16}$$

which describes the probability for one condensation nucleus to nucleate within some nucleation time t [see, e.g., *Lazaridis et al.*, 1992], can be used. We decided to use both the nucleation rate per particle (units s^{-1}) and the nucleation probability with nucleation time of 10^{-3} s to present our results of heterogeneous nucleation. Note that in this way of presenting J the number of CN is not directly seen in the value of J or P. Figure 1 shows two dust profiles (CN concentrations for $\tau = 0.1$, used in our study, and $\tau = 0.4$, moderate dust load) representative of Mars outside dust storms. The dust profiles are defined using the formulation of *Conrath* [1975] and will be discussed also in section 4. The number of activated CN is the product of CN concentration and the nucleation rate per particle shown in later figures. Note also that since the maximum value of P is unity P in the figures stays constant after reaching that value on the axis.

2.6. Differences Between Theories

[19] We have now described two ways of calculating the heterogeneous nucleation rate. Here, we discuss briefly the main differences between the theories and why we have selected surface diffusion as our technique.

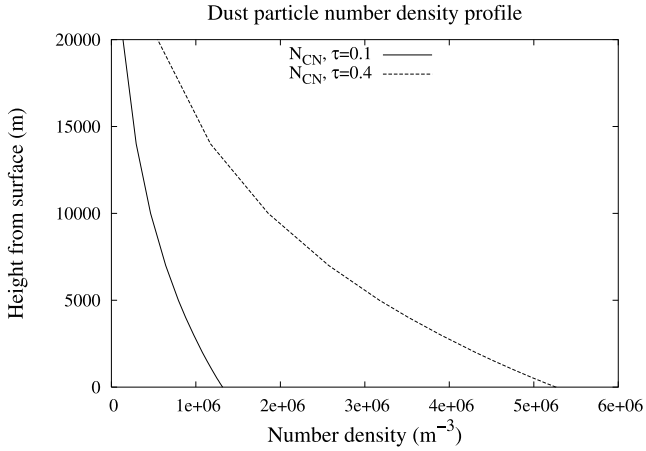

Figure 1. The dust profile calculated with visible optical depth values $\tau = 0.1$ and $\tau = 0.4$ and the formulation of *Conrath* [1975].

[20] The direct vapor deposition theory assumes that the embryo grows only by the vapor monomers colliding and adhering directly to the embryo. The surface diffusion approach also takes into account the collisions and adhering of monomers to the surface of the CN. Thus the nucleation rate includes both the direct collisions of the monomers on the embryo and the diffusion of the monomers on the surface into the embryo. Concentrations of monomers on the CN surface can be calculated in two ways. In the formulation of *Inada* [2002], the CN is assumed to be entirely covered with a layer of monomers, i.e., it is assumed to be completely wet with monomers (equation (13)). In the surface diffusion approach, the concentration is calculated as a steady-state between incoming and outgoing monomer fluxes (equation (7)).

[21] The difference between the direct vapor deposition and surface diffusion approaches for the nucleation rate is of the order of $\exp[(\Delta F_{des} - \Delta F_{sd})/kT]$, with the surface diffusion rate being about 10^5–10^8 faster than the direct vapor deposition in our temperature range. We have calculated nucleation rates in four cases, using two approaches for J and two for the surface monomer concentration with a simple monodisperse particle distribution. The results for the different theoretical approaches with a particle size of 1.0 μm are shown in Figures 2a and 2b. As expected, surface diffusion is the most efficient nucleation mechanism, and the more monomers on the CN (monolayer versus steady-state), the faster the nucleation. Thus the fastest nucleation rate is achieved with surface diffusion using monolayer concentration (SD+ML in Figure 2a). The second fastest rate is the approach used in this study: surface diffusion with steady-state concentration (SD+SS). The approach of *Inada* [2002], direct vapor deposition with monolayer concentration (DVD+ML), is about 10^8 times slower than our approach, and direct vapor deposition with steady-state concentration (DVD + SS) results in the slowest nucleation rate. The effect of monomer concentration is seen clearly, as is the difference between the two approaches for nucleation rate. However, the variation in nucleation probabilities between the different cases is not so large (Figure 2b).

[22] The effect of particle radius was explored by changing the particle size from 10 nm to 100 nm and from 1 μm to 10 μm. The results are presented in Figure 3. It seems that for CN sizes bigger than 100 nm the values of J and the critical saturation ratio for nucleation to be significant do not differ much. Major differences appear only with particle sizes below 100 nm.

[23] Since the difference in the nucleation rates is large, we need to consider which theoretical approach to choose. The surface diffusion approach, which yields the faster nucleation rates, is in our opinion more realistic as it takes into account monomers colliding on the entire surface of the CN. It provides an upper bound for the nucleation rate. This approach has been less popular in the literature since the necessary energies of surface diffusion and adsorption have been difficult to determine [*Lazaridis et al.*, 1991]. However, with measurement data

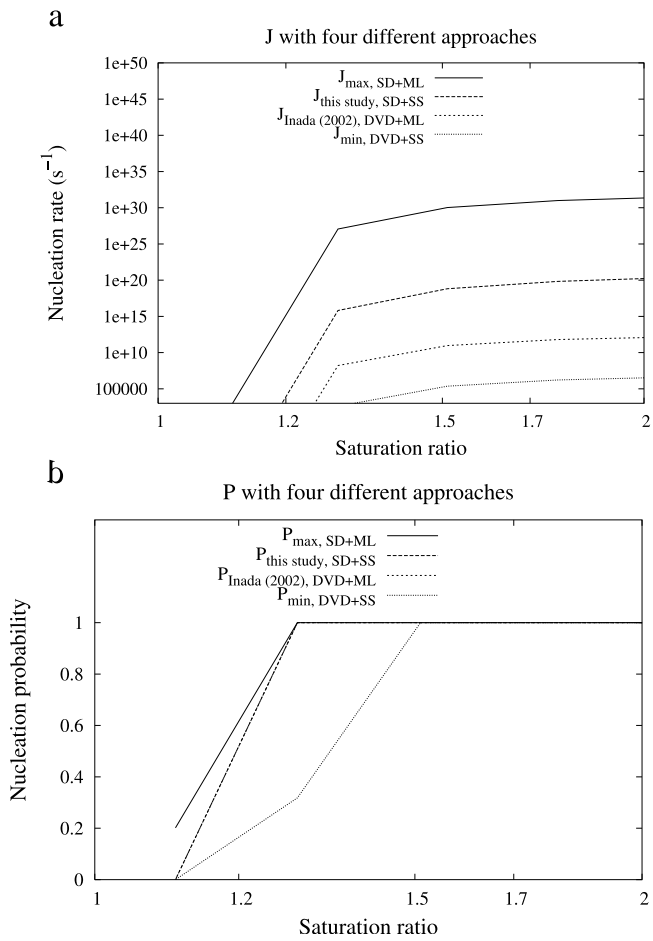

Figure 2. Comparison of different approaches for calculating the nucleation rate and defining the monomer concentration on the surface of the CN. (a) Nucleation rate per particle (s^{-1}) as a function of saturation ratio. (b) Nucleation probability as a function of saturation ratio. SD, surface diffusion approach; DVD, direct vapor deposition approach; ML, monolayer concentration; SS, steady-state concentration. See text for details. Note that nucleation probability stays constant after reaching the maximum value of 1 and that in Figure 2b the SD+SS and DVD+ML lines overlap each other.

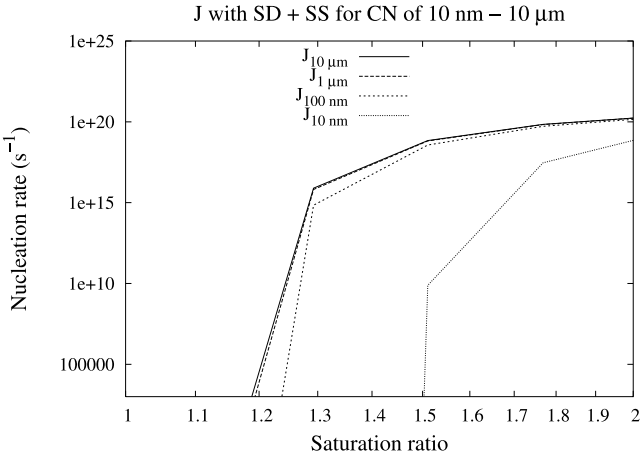

Figure 3. Effect of CN size on the nucleation rate using the theoretical approach of this study (surface diffusion with steady-state concentration of monomers). The continuous line describes nucleation rate as a function of the saturation ratio for r_{CN} = 10 μm, the long dashed line is for r_{CN} = 1 μm, the short dashed line is for r_{CN} = 100 nm, and the dotted line is for r_{CN} = 10 nm.

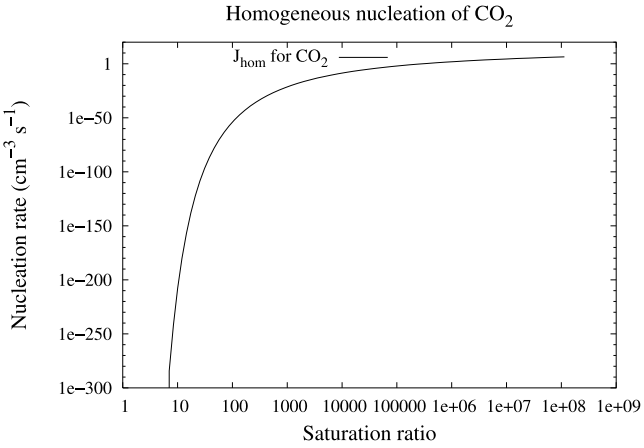

Figure 4. Homogeneous nucleation rate of CO_2 (cm^{-3} s^{-1}) on Mars under near-surface conditions.

becoming increasingly available, this approach can be recommended.

3. Basic Results

[24] Here, we present the basic results of the simulations in Martian near-surface conditions (p_{atm} = 600 Pa) with the atmospheric composition as described in Table 2. We kept the water vapor concentration at the average value of 300 ppmv, and thus the saturation ratio changed with changing temperature. The radius of the CN in the heterogeneous cases was set at 1 μm, which is close to the average effective radius of Martian dust distributions acquired from different observations [*Tomasko et al.*, 1999]. *Colaprete et al.* [1999] and *Inada* [2002] used values of 1.5 μm and 1.85 μm, respectively, for the effective radius. *Wood* [1999] used a value of 0.1 μm for the r_{CN} in his nucleation simulations. The nucleation rate is naturally sensitive to the size of the CN, decreasing rapidly for small CN, but leveling off for larger CN. We tested the effect of CN size on nucleation rates. In our simulations, the nucleation rate decreased rapidly for particles smaller than 1 μm. The effective (or cross-section weighted mean) radius of dust derived from observations of Mars Pathfinder (1.6 μm [*Tomasko et al.*, 1999]) is not sensitive to the number of smallest particles, which is the case also for the overall heterogeneous nucleation rate. The distribution with a small variance (effective radius r_{eff} = 1.6 μm and variance b = 0.2) described for the Martian dust by *Tomasko et al.* [1999] suggests that the dust distribution has only a small number of submicrometer particles for which the nucleation rate would be significantly lower. However, if the variance were larger than 0.2, e.g., b = 0.49, the amount of submicrometer particles would be three orders of magnitude higher for 10-nm particles and up to six orders of magnitude higher for 1-nm particles. The variances obtained from observations do differ from case to case so the most realistic size distribution is still speculative. The amount of small particles may be underestimated when a small variance is defined for the dust size distribution. However, the average effective radius has been around 1–2 μm in all observations. Thus our chosen CN size and the results obtained can be considered a fair first trial of the average conditions at least in the low latitudes on Mars. In this study we use the same CN size also for the polar cases to make results comparable.

Table 2. Atmospheric Composition Used in the Model Runs[a]

Gas	Symbol	Proportion
Carbon dioxide	CO_2	95.32%
Nitrogen	N_2	2.7%
Argon	Ar	1.6%
Oxygen	O_2	0.13%
Water vapor	H_2O	0.03%

[a]Composition (in vol%) is from *Owen* [1992]. Gases with very low concentrations (Ne, Kr, Xe, O_3) are omitted.

3.1. Homogeneous Cases

[25] Homogeneous nucleation of CO_2 is not possible in the present Martian atmosphere, as suggested and evaluated by *Wood* [1999] and *Colaprete and Toon* [2003]. Our results confirm this, and the same also appears to hold for H_2O. The results for the nucleation rates for both substances are shown in Figures 4 and 5. If the nucleation rate of J = 10^6 s^{-1} cm^{-3} is considered the critical limit above which nucleation becomes significant, this level is reached in our results with critical saturation ratios S_{crit} of about 10^5 and 10^7 for H_2O and CO_2, respectively. With constant vapor concentrations (Table 2), the temperatures corresponding to the critical saturation ratios are about 151 K and 81 K, respectively. The critical saturation ratios decrease about two orders of magnitude if we choose J = 1 s^{-1} cm^{-3} as the limiting value. The lowest temperatures measured in the Martian atmosphere are 129 K in the polar night at around 50 Pa by Viking Infrared Thermal Mapper (IRTM) [*Kieffer et al.*, 1976, 1977] and 95 K at a height of about 80 km by Mars Pathfinder [*Schofield et al.*, 1997]. For homogeneous nucleation of CO_2, the temperatures would always appear be too high in the light of observations. It should also be noted that our values of S_{crit} are for near-surface conditions. The vapor

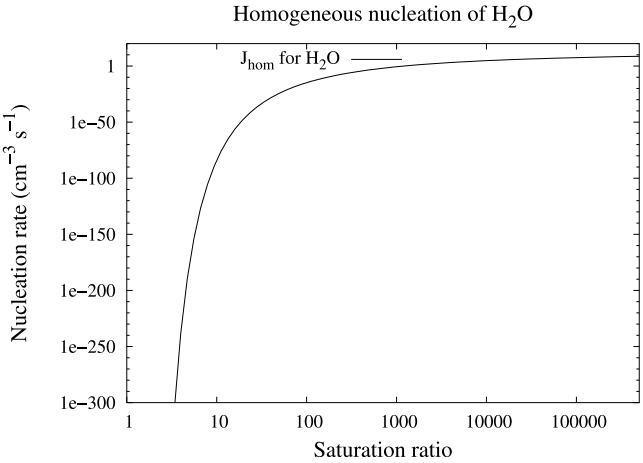

Figure 5. Homogeneous nucleation rate of H_2O (cm^{-3} s^{-1}) on Mars under near-surface conditions.

densities, and thus the temperature for nucleation, decrease with altitude. Therefore, as also noted by *Wood* [1999], although low temperatures are observed at high altitudes, the vapor density is too small to achieve sufficiently large saturation ratios for homogeneous nucleation of H_2O.

3.2. Heterogeneous Cases

[26] Both *Wood* [1999] and *Colaprete and Toon* [2002, 2003] have evaluated heterogeneous nucleation to be the primary mechanism for cloud formation on Mars. Theoretically, heterogeneous nucleation is always thermodynamically favored to homogeneous nucleation, given that condensation nuclei are available.

[27] Our main results for heterogeneous nucleation are presented in Figures 6 and 7. The critical saturation ratio for the nucleation probability P to be unity (meaning that all CN are activated within nucleation time $t = 10^{-3}$ s) is around 1.32 for CO_2 and 1.18 for H_2O. These correspond to temperatures of about 145 K for constant 95.3% concentration of CO_2 and about 200 K for a water vapor concentration of 300 ppmv. Such temperatures frequently occur in the Martian atmosphere, and both CO_2 and H_2O clouds and fogs are observed on Mars. In section 4, we describe studies of the height dependency of nucleation at some sites on Mars where clouds or fogs have been observed.

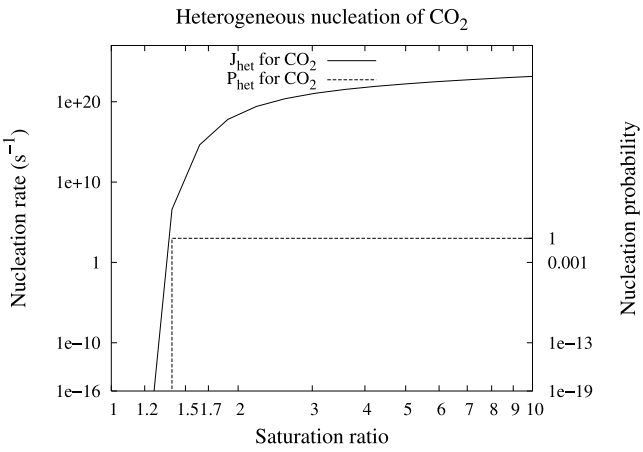

Figure 6. Heterogeneous nucleation rate per particle (s^{-1}, left y axis) and nucleation probability (right y axis) of CO_2 as a function of saturation ratio on Mars under near-surface conditions. Note that nucleation probability stays constant after reaching the maximum value of 1.

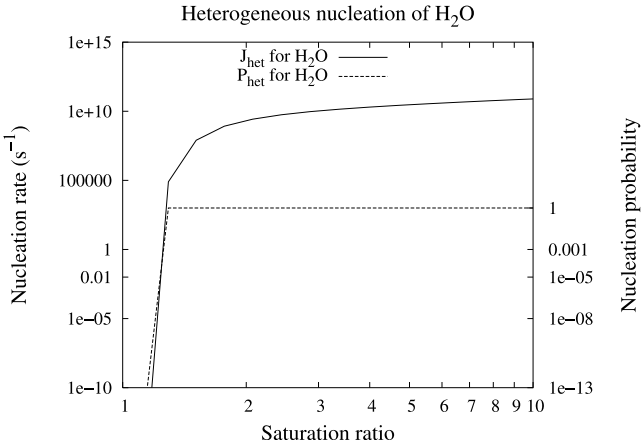

Figure 7. Heterogeneous nucleation rate per particle (s^{-1}, left y axis) and nucleation probability (right y axis) of H_2O as a function of saturation ratio on Mars under near-surface conditions. Note that nucleation probability stays constant after reaching the maximum value of 1.

[28] We compared our H_2O nucleation results with those of *Inada* [2002], who used a different approach for calculating the nucleation rate (the direct vapor deposition with monolayer coverage described previously). We tested our model by removing the differences between the two theoretical approaches and acquired almost identical results. The only remaining difference, the description of the CN distribution, caused a difference of less than 10^2 in nucleation rates. This is explained by *Inada* [2002] using a modified gamma distribution with an effective radius of 1.85 μm and variance of 0.25, while our CN distribution is monodisperse with a radius of 1.0 μm, as described at the beginning of section 3.

[29] We also compared our model to the results of *Glandorf et al.* [2002], who measured critical saturation ratio for CO_2 nucleation on water ice and derived the contact parameter from the results. We acquired nearly the same results for the critical saturation ratio by using their temperatures and contact parameters in our model. However, our critical saturation ratios were slightly lower than those they measured in every case. This can be explained by our different approaches. *Glandorf et al.* [2002] used a planar surface, pure CO_2 vapor, and an isothermal assumption (since the measurement set-up was designed to minimize nonisothermal effects). These factors anyhow affect in lowering the critical saturation ratio. The difference causing the discrepancy of results is in the formula of nucleation rate, where they used a constant kinetic prefactor calculated for one temperature and pressure and for a monolayer coverage of CO_2 on the surface. If our model calculates the kinetic prefactor independently but omits nonisothermal effects, we acquire an S_{crit} of 1.29 and a kinetic prefactor of $6.2 \cdot 10^{31}$ compared with the value of 10^{27} that *Glandorf et al.* [2002] used. Our model takes into account curvature and nonisothermal effects, has a realistic composition of the

Table 3. Parameters of the Model Runs of the Height Dependency of the Nucleation Rate[a]

Location	Φ, °N	λ, °W	L_s, °	V_g, m s^{-1}	PWC, μm	T_s, K	p_s, hPa	α	I, J m^{-2} s$^{-1/2}$ K^{-1}	Profile
Pathfinder	19.3	33	150	2.5	19	202	6.79	0.17	390	MCD+1D
Memnonia	−15.0	145	99	3.6	11.3	166	6.93	0.13	283	MCD+1D
North polar hood	82.5	15	290		0	150	8.84			MCD
South polar hood	−82.5	15	120		0	145	4.1			MCD

[a]The comparison with *Colaprete et al.* [1999] is explained only in the text. Φ, latitude; λ, longitude; L_s, areocentric longitude (season, explained in text); V_g, geostrophic (prevailing) wind speed; PWC, precipitable water content (integrated amount of water in the air column); T_s, surface temperature; p_s, surface pressure; α, surface albedo; I, thermal inertia of the soil.

atmosphere, and calculates the kinetic prefactor for each temperature and pressure. If these differences are eliminated from our model, we get values closer to theirs, but the average critical saturation ratio remains lower, 1.32 compared with their 1.34.

4. Nucleation as a Function of Height in the Martian Atmosphere and Comparison With Other Models and Observations

[30] We conducted studies on nucleation in the Martian atmosphere as a function of height in selected locations. We chose places such as the Mars Pathfinder landing site and the polar areas, where ice clouds or surface fogs have been observed.

[31] The sites chosen are listed in Table 3. Mars Pathfinder (MPF) observations suggest that near-surface fog forms during the early morning hours [*Schofield et al.*, 1997]. This has also been modeled by *Savijärvi* [1999]. Thus we chose the MPF landing site (19°N, 33°W, L_s = 143°) for our study. We also tested our model with the Mars Pathfinder entry profile and compared our results with those of *Colaprete et al.* [1999]. In the Memnonia region (15°S, 145°W, L_s = 99°), surface fogs were also observed by Viking Orbiter 1 [*Briggs et al.*, 1977]. We chose two regions (see Table 3) as representative places for polar hoods which are composed of both H_2O and CO_2 clouds. We conducted simulations on the formation of CO_2 clouds in midwinter when all water vapor has already condensed onto the polar cap. The areocentric longitude L_s describes the season on Mars; L_s = 0° is the northern spring equinox, L_s = 90° the northern summer solstice, L_s = 180° the northern autumn equinox, and L_s = 270° the northern winter solstice.

[32] One important factor to be taken into account is that the dust size distribution changes in reality with height because of deposition caused by turbulence and gravitational settling (and possibly coagulation). This is parameterized in our nucleation profile simulations by scaling the surface value of the dust radius with a factor derived from previous studies and new modeling results. According to the findings of *Colaprete et al.* [1999], the mode radius of the dust size distribution shifts only slightly up until 30 km or so during a 4-sol (Martian day) simulation. We simulated the change of dust size with height with the deposition model of *Merikallio* [2003], which calculates the gravitational Stokes deposition velocity also incorporating the Cunningham correction factor. Vertical changes in gravitational acceleration, pressure, temperature, and viscosity are also taken into account. The deposition model simulations were done using the polar MCD profiles and the Mars Pathfinder entry profile. The simulations confirmed that the linear decrease of the dust radius with a factor of 2 from 0 to 20 km is a fair first approximation. This is included in the nucleation model simulations. From a practical viewpoint, this has no impact on surface fog formation, but with cloud formation higher up in the atmosphere the change in dust radius can have a significant effect.

4.1. Mars Pathfinder and Memnonia

4.1.1. Profiles

[33] For the Mars Pathfinder (19°N, 33°W, L_s = 143°, section 4.1.2) and Memnonia (15°S, 145°W, L_s = 99°, section 4.1.3), the same methods were used to acquire the atmospheric profiles, and these are described in the following. From the Mars Climate Database (MCD) [*Lewis et al.*, 1999], which is a database based on general circulation model simulations of the Martian climate, it is possible to obtain average atmospheric profiles for different locations on Mars. The model and database variables do not, however, include moisture. The model used to create the database also assumes immediate CO_2 condensation after saturation is reached, and thus does not allow the temperature to fall below the saturation temperature.

[34] To acquire representative atmospheric profiles including moisture, we used the one-dimensional Mars model (1-D model) of the University of Helsinki [*Savijärvi*, 1999]. This boundary layer model includes a water cycle with a simple scheme for condensation, which was switched off to obtain the cloudless moisture profiles. The moisture profile in the 1-D model is initialized with a vertically constant relative humidity, which then changes during the simulations with turbulent mixing. The boundary layer processes in the model are further discussed in the Pathfinder case by *Määttänen and Savijärvi* [2004]. We initialized the 1-D model with the temperature profiles acquired from MCD, ran the simulations for 3 sols (Martian days), in which time the model converged, and used the profiles from the third sol for running the nucleation model. The atmospheric water vapor amounts have been compared with the observations of total Martian atmospheric water content from the Thermal Emission Spectrometer (TES) onboard the Mars Global Surveyor [*Smith*, 2002]. The initial relative humidity in the 1-D model was set to a value that resulted in an integrated water vapor amount (precipitable water content) representative for each location according to the TES observations. The thermal inertia I is also based on observations from TES [*Mellon et al.*, 2000; *Christensen et al.*, 2001].

[35] The amount of dust varies so little in these locations according to the infrared optical depth measurements by TES [*Smith et al.*, 2001] that a constant value of 0.1 for the visible optical depth τ was used. This value is fairly low even for low atmospheric dust load but was chosen to make

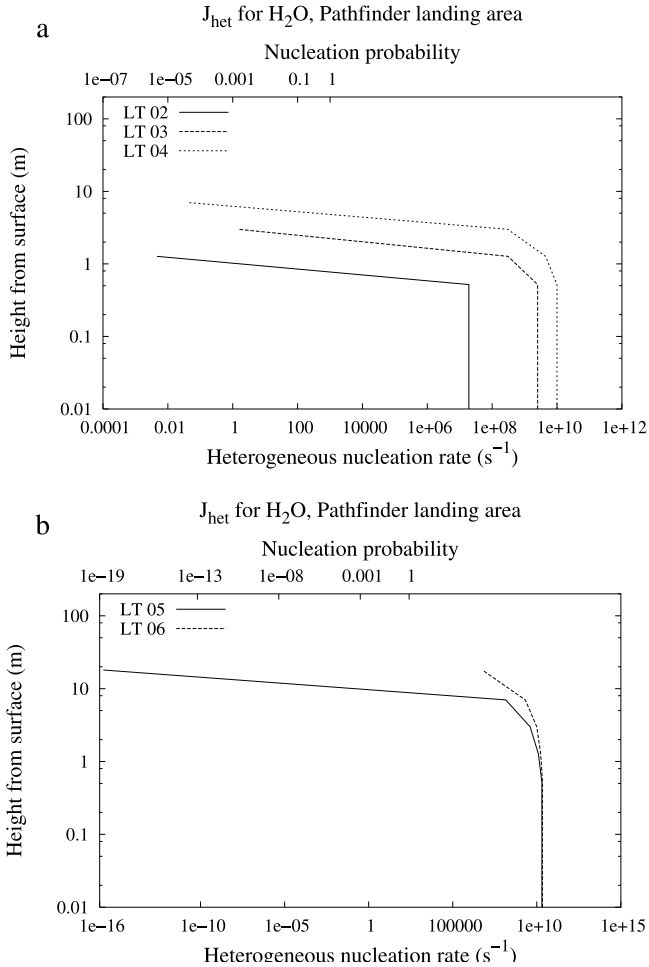

Figure 8. Heterogeneous nucleation rate per particle (s^{-1}, bottom x axis) and nucleation probability (top x axis) of H_2O as a function of height (y axis) in the Mars Pathfinder landing area (19°N, 33°W, L_s = 143°). Note that nucleation probability stays constant after reaching the maximum value of 1. (a) Local times (LT) 02–04; (b) LT 05–06.

all of our simulations comparable (for the basic cases, this value was chosen from the work of *Wood* [1999]). Dust is included in the 1-D model only in the radiative part and described with the help of visible optical depth. The vertical profile $\tau(z)$ is as defined by *Conrath* [1975] (Figure 1). In the layer closest to the surface, the number density of dust particles is defined as $N_{CN} = \tau/(Q\pi H) \cdot (1/r_{CN}^2)$, where τ is the dust optical depth, Q the Mie extinction coefficient (2.42 [*Wood*, 1999]), H the scale height (10 km [*Wood*, 1999]), and r_{CN} the radius of the dust particles.

[36] We ran the nucleation models on each 1-D model level, getting profiles of nucleation rates ((*J*, *z*) -plots) as a result, which were then compared with fog observations in the Pathfinder and Memnonia cases.

[37] For the Pathfinder case, we also present a comparison with *Colaprete et al.* [1999] using their Mars Pathfinder entry profile, which was not modified in any way.

4.1.2. Mars Pathfinder

[38] The results for the Mars Pathfinder Lander are shown in Figures 8a and 8b. Supporting the model results of *Savijärvi* [1999], we confirm that water ice fog formation is possible since new ice particles are formed near the surface to about a height of 20 m. The 1-D model of *Savijärvi* [1999] produced fog up to 40 m. The most plausible explanation for the discrepancy in results is that the 1-D model of *Savijärvi* [1999] assumed excess vapor to condense into ice crystals right after saturation is reached (at a relative humidity of 100%), whereas our results show (see section 3.2) that particle formation actually takes place only after relative humidity exceeds 118%. Thus, in our model, the fog formation is restricted closer to the surface, where the temperatures are sufficiently cold.

[39] *Colaprete et al.* [1999] modeled water ice cloud formation using the entry profile acquired by the Mars Pathfinder Lander (above 8 km). They found that clouds should form on higher levels in the atmosphere but did not specifically model the surface fog at the landing site.

[40] We obtained the MPF entry profile from A. Colaprete (personal communication). In addition, their values for the contact parameter of heterogeneous nucleation *m* (0.95), water vapor mixing ratio (70 ppmv), and dust parameters including the optical depth (0.5), scale height (12.5 km), and effective radius (1.5 μm) as the near-surface value for the CN size were used. Our model predicted H_2O nucleation (Figure 9) at around the same heights as in *Colaprete et al.* [1999]. Their model includes, however, all of the important aerosol processes in the Martian atmosphere, these being nucleation, condensation, and sedimentation. Their dust profile was allowed to evolve for 4 sols with sedimentation before introducing the other aerosol processes. We described the change in dust size with height with the linear decrease described earlier. They also modeled the whole diurnal cycle, while we only tested the results for the entry profile. The results are nevertheless qualitatively very close to each other at 55 km and below.

4.1.3. Memnonia

[41] We studied the Memnonia region as in *Inada* [2002], and our results show water ice nucleation in a thick layer

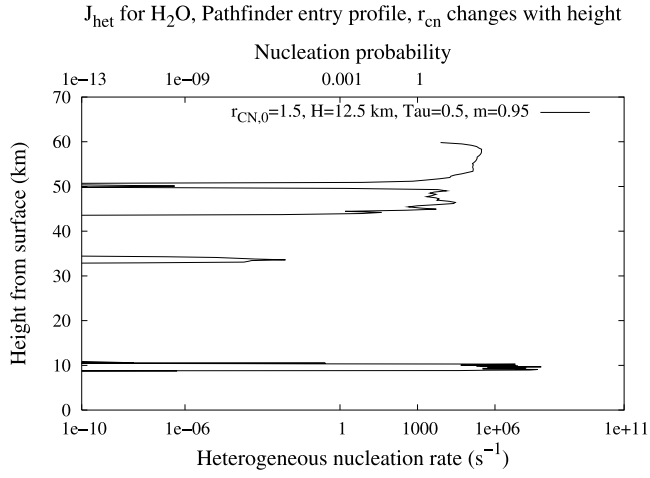

Figure 9. Heterogeneous nucleation rate per particle (s^{-1}, bottom x axis) and nucleation probability (top x axis) of H_2O as a function of height (y axis) for the Pathfinder entry profile. Temperature measurements do not reach below 8 km. Note that nucleation probability stays constant after reaching the maximum value of 1.

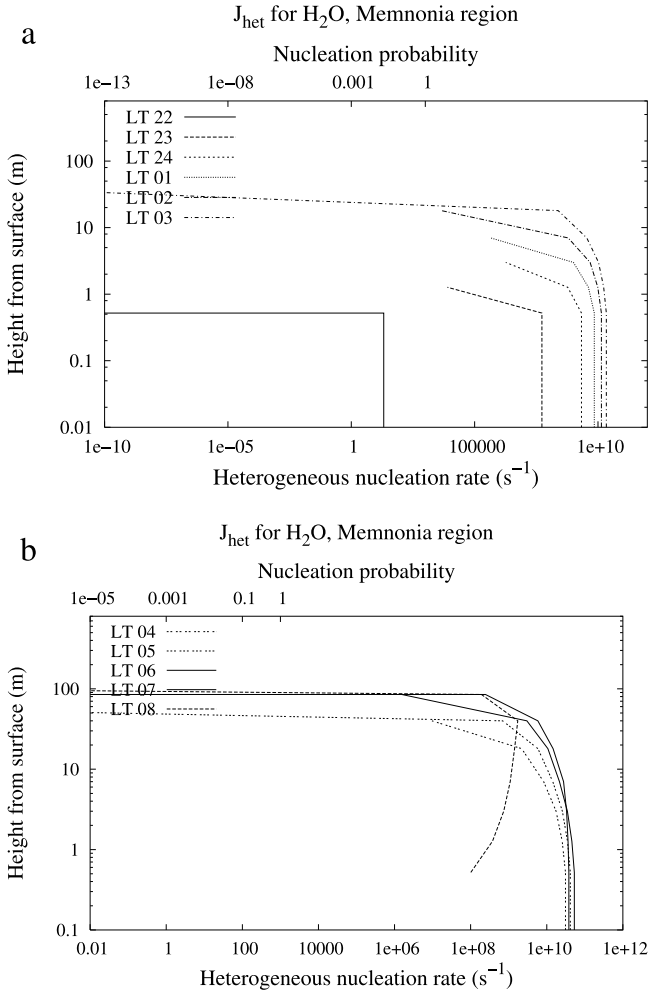

Figure 10. Heterogeneous nucleation rate per particle (s^{-1}, bottom x axis) and nucleation probability (top x axis) of H_2O as a function of height (y axis) in the Memnonia area (15°S, 145°W, L_s = 99°, orbiter observations of a surface fog). Note that nucleation probability stays constant after reaching the maximum value of 1. (a) Local times (LT) 22–03; (b) LT 04–08.

near the surface (Figures 10a and 10b). Nucleation begins close to the surface at 22 local time (LT) and continues in a 100-m-thick layer until 08 LT, after which it stops because of a temperature increase due to sunrise. In *Inada* [2002], the saturated conditions for water started at around 19 LT, the entire atmosphere below 800 m was saturated until 07 LT, and saturated conditions continued until noon in the lowest layer. According to our results, the critical saturation ratio for water ice nucleation to initiate is around 1.18, which is why we do not predict nucleation in the saturated 800-m layer.

4.2. Polar Winter Simulations

[42] In the autumn, when the temperature starts to decrease polar hood clouds develop; they cover the cold polar caps of Mars [*Hunt and James*, 1985], exhibit a variety of cloud types, and are formed of both H_2O and CO_2 ice particles. Formation of polar hood H_2O clouds is related to the increase in weather system activity in storm tracks [*Tamppari et al.*, 2003]. *Tamppari et al.* [2003] observed H_2O clouds in the early autumn southward of 60°N, which are related to the onset of the storm season and this polar hood development. The Mars Orbiter Laser Altimeter (MOLA) observed echoes in the polar areas most probably caused by CO_2 clouds [*Pettengill and Ford*, 2000; *Ivanov and Muhleman*, 2001]. Such clouds have been modeled by, e.g., *Colaprete and Toon* [2002], *Colaprete et al.* [2003], and *Tobie et al.* [2003]. We concentrated on midwinter CO_2 cloud cases since the temperatures during the polar night are sufficiently cold for CO_2 to condense into clouds and surface frost.

[43] We chose two wintertime polar CO_2 cloud cases, one northern and the other southern. For the polar winter simulations, we used unmodified MCD profiles. Because of the low temperatures, in our simulations we presume that all water vapor has already condensed onto the polar cap, and thus the moisture profile was not needed. Also, since in the polar winter night the boundary layer is very stable and mixing is negligible, the 1-D model would not have made much diurnal difference to the profiles.

[44] In both cases, the atmosphere does not reach the saturated state, neither the critical saturation ratio needed for CO_2 nucleation. This is not surprising since the MCD profiles are adjusted not to exceed CO_2 saturation. However, according to our studies, such an assumption of instant condensation at saturation is too simplified, also making these profiles inapplicable in cloud formation studies. Very low temperatures have been observed in the polar night already by Viking IRTM instrument [*Kieffer et al.*, 1976, 1977] revealing the presence of temperatures below CO_2 saturation. Later observations of polar clouds by MOLA revealed the presence and wavelike structure of the polar clouds [*Pettengill and Ford*, 2000; *Ivanov and Muhleman*, 2001], giving a hint about their formation mechanism.

[45] *Tobie et al.* [2003] suggested that orographic waves are required for creating temperature perturbations sufficiently large for CO_2 nucleation. Their model results showed that temperature perturbations of about 2 K via adiabatic cooling were needed in the lower atmosphere for the initial saturated state to reach an adequately high supersaturation. *Colaprete and Toon* [2002, 2003] and *Colaprete et al.* [2003] also modeled the formation of CO_2 clouds in the Martian atmosphere and concluded that a temperature decrease of several degrees below the CO_2 saturation temperature is required for the onset of cloud formation and that in most cases the driving force for CO_2 cloud formation would be of dynamic origin, such as wave activity or convection, causing the extra cooling needed.

5. Conclusions and Summary

[46] We have constructed models and conducted simulations on nucleation in the Martian atmosphere. Homogeneous nucleation seems very unlikely because of the high supersaturations required. Condensation nuclei are, on the other hand, abundant because of the ubiquitous dust. Even with a low dust load of the atmosphere and a visible optical depth of τ = 0.1, the surface number concentration of the CN is 10^6 m^{-3}. Therefore heterogeneous nucleation is possible and indeed likely. The critical saturation ratio for

heterogeneous nucleation to start is around 1.18 for H_2O and 1.32 for CO_2. Nonisothermal effects are important in the 95% CO_2 atmosphere since CO_2 nucleation occurs in a near-pure vapor, and even for water the nonisothermality has a small effect at high temperatures.

[47] According to our studies, the approach chosen for calculating the nucleation rate can have a significant effect on the magnitude of the results under Martian conditions. The values of nucleation rates with different approaches vary much more than do the nucleation probabilities. Differences in approaches should be taken into account when comparing results of different studies.

[48] With atmospheric model simulations for the time-height dependency of the Martian lower atmosphere, we predicted water ice nucleation in both the Mars Pathfinder landing area and the Memnonia region, where morning surface fogs have been observed [*Briggs et al.*, 1977; *Schofield et al.*, 1997]. Using the Mars Pathfinder entry profile, we predicted nucleation at around the same heights where *Colaprete et al.* [1999] modeled clouds.

[49] In the polar areas, the atmosphere does not reach CO_2 saturation according to our nucleation model using the average MCD profiles which do not allow for supersaturated state. The assumption of immediate CO_2 condensation at saturation is an oversimplification according to our studies. Temperatures colder than the saturation have been observed already by Viking IRTM [*Kieffer et al.*, 1976, 1977] revealing the existence of supersaturated state and the possibility of CO_2 clouds in the polar night. Also MOLA observed polar clouds with a wavelike structure [*Pettengill and Ford*, 2000; *Ivanov and Muhleman*, 2001] suggesting an effect of a dynamical phenomenon in the formation process. Later studies [e.g., *Colaprete and Toon*, 2002, 2003; *Tobie et al.*, 2003] have shown that cloud formation in the polar areas would seem to require negative temperature perturbations of several degrees caused by adiabatic cooling in, for example, orographic waves or convective plumes to ensure that the necessary supersaturations are reached.

[50] **Acknowledgments.** Financial support from the Academy of Finland is gratefully acknowledged. We also thank Anthony Colaprete for providing the Mars Pathfinder entry profile data.

References

Briggs, G., K. Klaasen, T. Thorpe, and J. Wellman (1977), Martian Dynamical Phenomena During June–November 1967: Viking Orbiter Imaging Results, *J. Geophys. Res.*, *82*(28), 4121–4149.

Buck, A. L. (1981), New equations for computing vapour pressure and enhancement factor, *J. Appl. Meteorol.*, *20*, 1527–1532.

Christensen, P. R., et al. (2001), Mars Global Surveyor Thermal Emission Spectrometer experiment: Investigation description and surface science results, *J. Geophys. Res.*, *106*(E10), 23,823–23,872.

Colaprete, A., and O. B. Toon (2002), Carbon dioxide snow storms during the polar night on Mars, *J. Geophys. Res.*, *107*(E7), 5051, doi:10.1029/2001JE001758.

Colaprete, A., and O. B. Toon (2003), Carbon dioxide clouds in an early dense Martian atmosphere, *J. Geophys. Res.*, *108*(E4), 5025, doi:10.1029/2002JE001967.

Colaprete, A., O. B. Toon, and J. A. Magalhães (1999), Cloud formation under Mars Pathfinder conditions, *J. Geophys. Res.*, *104*(E4), 9043–9054.

Colaprete, A., R. M. Haberle, and O. B. Toon (2003), Formation of convective carbon dioxide clouds near the south pole of Mars, *J. Geophys. Res.*, *108*(E7), 5081, doi:10.1029/2003JE002053.

Conrath, B. J. (1975), Thermal structure of the Martian atmosphere during the dissipation of dust storm of 1971, *Icarus*, *24*, 36–46.

Feder, J., K. C. Russell, J. Lothe, and G. M. Pound (1966), Homogeneous nucleation and growth of droplets in vapours, *Adv. Phys.*, *15*, 111–178.

Fletcher, N. H. (1958), Size effect in heterogeneous nucleation, *J. Chem. Phys.*, *29*(3), 572–576.

Glandorf, D. L., A. Colaprete, M. A. Tolbert, and O. B. Toon (2002), CO_2 Snow on Mars and early Earth: Experimental constraints, *Icarus*, *160*, 66–72.

Hunt, G. E., and P. B. James (1985), Martian cloud systems: Current knowledge and future observations, *Adv. Space Res.*, *5*(8), 93–99.

Inada, A. (2002), Simulations of Martian surface fog and calibration of Mars Imaging Camera for its future observations, Ph.D. thesis, Kobe University, Kobe, Japan.

Ivanov, A. B., and D. O. Muhleman (2001), Cloud reflection observations: Results from the Mars Orbiter Laser Altimeter, *Icarus*, *154*, 190–206.

Kasting, J. F. (1991), CO_2 condensation and the climate of early Mars, *Icarus*, *94*, 1–13.

Keesee, R. G. (1989), Nucleation and particle formation in the upper atmosphere, *J. Geophys. Res.*, *94*(D12), 14,683–14,692.

Kieffer, H. H., S. C. Chase, E. D. Miner, F. D. Palluconi, G. Munch, G. Neugebauer, and T. Z. Martin (1976), Infrared thermal mapping of the Martian surface and atmosphere: First results, *Science*, *193*, 780–786.

Kieffer, H. H., T. Z. Martin, A. R. Peterfreund, B. M. Jakosky, E. D. Miner, and F. D. Palluconi (1977), Thermal and albedo mapping of Mars during the Viking primary mission, *J. Geophys. Res.*, *82*, 4249–4291.

Kulmala, M., A. Lauri, H. Vehkamäki, A. Laaksonen, D. Petersen, and P. E. Wagner (2001), Strange predictions by binary heterogeneous nucleation theory compared with a quantitative experiment, *J. Phys. Chem. B*, *105*, 11,800–11,808.

Lazaridis, M., M. Kulmala, and A. Laaksonen (1991), Binary heterogeneous nucleation of a water-sulphuric acid system: The effect of hydrate interaction, *J. Aerosol Sci.*, *22*, 823–830.

Lazaridis, M., M. Kulmala, and B. Z. Gorbunov (1992), Binary heterogeneous nucleation at a non-uniform surface, *J. Aerosol Sci.*, *23*(5), 457–466.

Lewis, S. R., M. Collins, P. L. Read, F. Forget, F. Hourdin, R. Fournier, C. Hourdin, O. Talagrand, and J.-P. Huot (1999), A climate database for Mars, *J. Geophys. Res.*, *104*(E10), 24,177–24,194.

Määttänen, A., and H. Savijärvi (2004), Sensitivity tests with a one-dimensional boundary-layer Mars model, *Boundary Layer Meteorol.*, *113*(3), 305–320.

Mellon, M. T., B. M. Jakosky, H. H. Kieffer, and P. R. Christensen (2000), High-resolution thermal inertia mapping from the Mars Global Surveyor Thermal Emission spectrometer, *Icarus*, *148*, 437–455.

Merikallio, S. (2003), Available solar energy on the dusty Martian atmosphere and surface, M.Sc. thesis (tech.), Helsinki Univ. of Technol., Helsinki.

Michelangeli, D. V., O. B. Toon, R. M. Haberle, and J. B. Pollack (1993), Numerical simulations of the formation and evolution of water ice clouds in the Martian atmosphere, *Icarus*, *100*, 261–285.

Owen, T. (1992), The composition and early history of the atmosphere of Mars, in *Mars*, edited by H. H. Kieffer et al., pp. 818–834, Univ. of Ariz. Press, Tucson.

Pettengill, G. H., and P. G. Ford (2000), Winter clouds over the north Martian polar cap, *Geophys. Res. Lett.*, *27*(5), 609–612.

Pruppacher, H. R., and J. D. Klett (1997), *Microphysics of Clouds and Precipitation*, Springer, New York.

Sanford, S. A., and L. J. Allamandola (1990), The physical and infrared spectral properties of CO_2 in astrophysical ice analogs, *Astrophys. J.*, *355*, 357–372.

Savijärvi, H. (1999), A model study of the atmospheric boundary layer in the Mars Pathfinder lander conditions, *Q. J. R. Meteorol. Soc.*, *125*, 483–493.

Savijärvi, H., A. Määttänen, J. Kauhanen, and A.-M. Harri (2004), Mars Pathfinder: New data and new model simulations, *Q. J. R. Meteorol. Soc.*, *130*, 669–684.

Schofield, J. T., J. R. Barnes, D. Crisp, R. M. Haberle, S. Larsen, J. A. Magalhaes, J. R. Murphy, A. Seiff, and G. Wilson (1997), The Mars Pathfinder Atmospheric Structure Investigation/Meteorology (ASI/MET) Experiment, *Science*, *278*, 1752–1757.

Seki, J., and H. Hasegawa (1983), The heterogeneous condensation of interstellar ice grains, *Astrophys. Space Sci.*, *94*, 177–189.

Smith, M. D. (2002), The annual cycle of water vapor on Mars as observed by the Thermal Emission Spectrometer, *J. Geophys. Res.*, *107*(E11), 5115, doi:10.1029/2001JE001522.

Smith, M. D., J. C. Pearl, B. J. Conrath, and P. R. Christensen (2001), One Martian year of atmospheric observations by the Thermal Emission Spectrometer, *Geophys. Res. Lett.*, *28*(22), 4263–4266.

Tamppari, L. K., R. W. Zurek, and D. A. Paige (2003), Viking-era diurnal water-ice clouds, *J. Geophys. Res.*, *108*(E7), 5073, doi:10.1029/2002JE001911.

Tobie, G., F. Forget, and F. Lott (2003), Numerical simulation of the winter polar wave clouds observed by Mars Global Surveyor Mars Orbiter Laser Altimeter, *Icarus*, *164*, 33–49.

Tomasko, M. G., L. R. Loose, M. Lemmon, P. H. Smith, and E. Wegryn (1999), Properties of dust in the Martian atmosphere from the Imager on Mars Pathfinder, *J. Geophys. Res.*, *104*(E4), 8987–9007.

Volmer, M. (1939), *Kinetik der Phasenbildung*, Von Theodor Steinkopff, Dresden, Germany.

Wood, S. E. (1999), Nucleation and growth of CO_2 ice crystals in the Martian atmosphere, Ph.D. thesis, Univ. of Calif., Los Angeles.

Zent, A. P., and R. C. Quinn (1995), Simultaneous adsorption of CO_2 and H_2O under Mars-like conditions and application to the evolution of the Martian climate, *J. Geophys. Res.*, *100*, 5341–5349.

J. Kauhanen, M. Kulmala, A. Lauri, A. Määttänen, H. Savijärvi, and H. Vehkamäki, Division of Atmospheric Sciences, Department of Physical Sciences, University of Helsinki, P.O. Box 64, Helsinki, FIN-00014 Finland. (anni.maattanen@helsinki.fi)

S. Merikallio, Space Research, Finnish Meteorological Institute, P.O. Box 503, Helsinki, FIN-00101 Finland.